

pubs.acs.org/JPCC Article

Strong Metal—Sulfur Hybridization in the Conduction Band of the Quasi-One-Dimensional Transition-Metal Trichalcogenides: TiS₃ and ZrS₃

Simeon J. Gilbert, Hemian Yi, Tula Paudel, Alexey Lipatov, Andrew J. Yost, Alexander Sinitskii, Evgeny Y. Tsymbal, Jose Avila, Maria C. Asensio, and Peter A. Dowben*



Cite This: J. Phys. Chem. C 2022, 126, 17647-17655

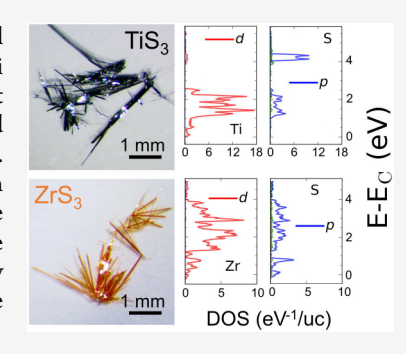


ACCESS

Metrics & More

Article Recommendations

ABSTRACT: The elemental contributions to the conduction bands of the transition-metal trichalcogenides TiS₃ and ZrS₃ were examined using X-ray absorption spectroscopy, at the Ti and S 2p edges and the Zr 3p edges. A comparative study of these two compounds shows that the bottom of the conduction band, for both TiS₃ and ZrS₃, is comprised mainly of hybridized transition metal—sulfur orbitals, either Ti 3d and S 3p orbitals or Zr 4d and S 3p orbitals. Density functional theory and experiment both indicate that the bottom of the conduction band, in the case of TiS₃, has the Ti 3d weight. Although weak, experiment indicates that the S-weighted contribution to the conduction band minimum for ZrS₃ is greater than in the case of TiS₃. For ZrS₃, theory, however, indicates that the conduction band is dominated by hybridization of the Zr 4d and S 3p orbitals, including in the vicinity of the bottom of the conduction band.



1. INTRODUCTION

The transition-metal trichalcogenides (TMTs) are an intriguing class of two-dimensional (2D) materials where edge scattering might be minimized with transistor widths on the scale of 10 nm or less. The transition-metal trichalcogenide class of materials, formed by 1D chains of covalently bound MX_3 (M = Ti, Zr, Hf, Nb; X = S, Se, Te) trigonal prisms, are held together by weak van der Waals forces to form 2D ¹³ Both TiS₃ and ZrS₃ crystallize in the ZrSe₃-type structure $(P2_1/m \text{ space group})$, in which transition-metal atoms (Ti or Zr) are surrounded by sulfur atoms, as schematically illustrated in Figure 1. Thus far, TiS₃ has received the most attention and has been investigated for use in field-effect transistors $^{6,7,14-20}$ and optoelectronics. $^{3,5,6,11-13,19-23}$ With the exception of TaS₃ and NbS₃, research into other TMTs has remained more limited. $^{4,19,20,24-30}$ As a semiconductor, TiS_3 is generally ntype, 4,7,14-17,25,31 with potentially extremely light mass carriers, where the conduction band edge is low lying enough with respect to the Fermi level that with sufficient gate voltage the TiS3 can be driven through a nonmetal-to-metal transition.¹⁷ Therefore, investigations into the electronic structure of the conduction band are extremely important to better understand the majority carrier transport. The optical properties of both TiS₃(100) and ZrS₃(100) are extremely light polarization dependent, 5,6,19,20,23,26,32-36 and recent reviews 19,20 have emphasized the optoelectronic properties. The anisotropic band structure and band symmetries of both the occupied and unoccupied bands clearly play a role in the

light polarization-dependent response of a phototransistor. ^{21,37} So there are increasing detailed experimental investigations of the occupied band structure ^{17,23,31,38} which should be complemented by experimental studies of the unoccupied band structure.

Detailed investigations into the conduction band orbital hybridization in the transition-metal trichalcogenides like TiS₃^{8,39,40} and ZrS₃⁴¹ remain sparse, nonetheless. In the absence of inverse photoemission, X-ray absorption spectroscopy (XAS) has been shown for the Ti 2p edge in TiS₃^{39,40} and for the S 2p edge in ZrS3, but the element specific density of states in the region above the Fermi level has not been experimentally investigated. Although, as summarized elsewhere, 19,20,23,31,38 there is a wealth of band structure calculations for TiS3 and ZrS3, in this paper, we provide insight into the unoccupied electronic states of two TMTs, TiS₃ and ZrS₃, through a comparison of X-ray absorption spectroscopy (XAS) and density functional theory (DFT); while inverse photoemission and XAS are comparable, 42 XAS has the advantage of elemental specificity. Through the first combined experimental and theoretical characterization of the

Received: August 5, 2022 Revised: September 24, 2022 Published: October 10, 2022





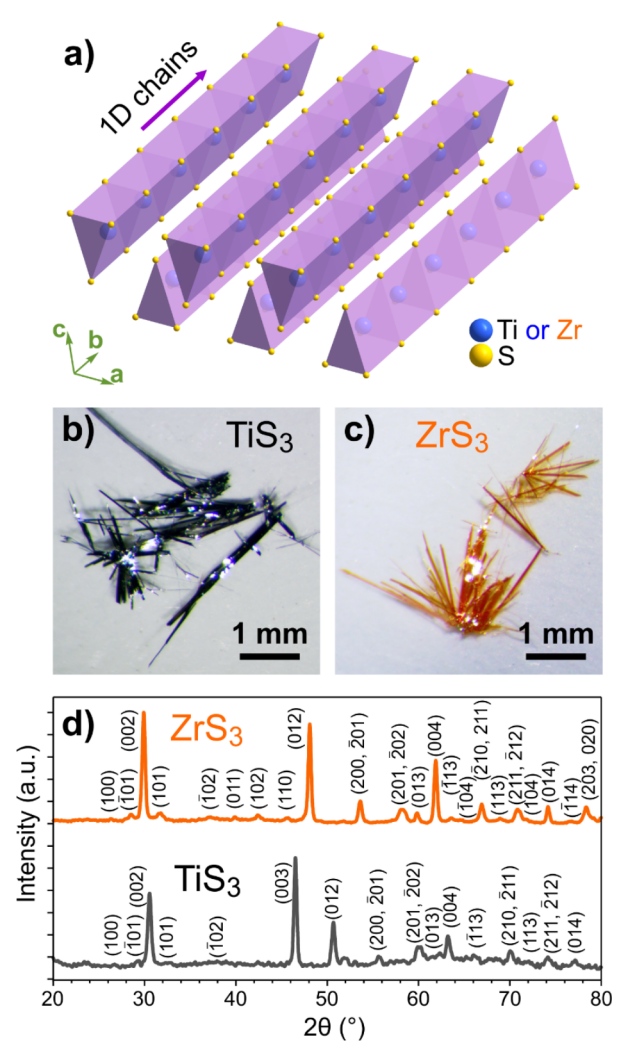


Figure 1. (a) Scheme of the TMT crystal structure showing 1D chains formed by trigonal sulfur prisms with transition-metal atoms (Ti or Zr) in the centers. (b, c) Optical images of the TiS_3 (b) and ZrS_3 (c) crystals grown for this study. (d) Powder XRD patterns of TiS_3 and ZrS_3 crystals.

unoccupied states in TiS_3 and ZrS_3 , we show that the conduction band structure, near the Fermi level of both materials, is composed largely of p-d hybridized orbitals.

2. METHODS

2.1. Experimental Details. Nanowhiskers of TiS_3 and ZrS_3 were synthesized using a direct reaction of titanium or zirconium with sulfur following previous studies. The synthesis of TiS_3 crystals was performed in vacuum-sealed ampules at 550 °C via the reaction between metallic titanium and sulfur vapor, as described in our previous works. The ZrS_3 crystals were also grown through the direct reaction of elemental precursors. In a typical synthesis, we combined ~ 0.1 g of Zr foil and ~ 0.115 g (corresponding to $\sim 10\%$ molar excess in stoichiometry) of sulfur powder, sealed the mixture in a quartz ampule under the pressure of ~ 200 mTorr, and annealed it at 650 °C for 2 weeks. The formation of TiS_3 and ZrS_3 was confirmed by powder X-ray diffraction (XRD) using a Difray 401 instrument with Cr $K\alpha$ radiation. The resulting XRD patterns for both TiS_3 and ZrS_3 are shown in Figure 1d.

All reflections were indexed according to the published crystallographic data for ${\rm TiS_3}^{15,43}$ and ${\rm ZrS_3}^{43}$ demonstrating the formation of pure TMT phases, while the critical points obtained from prior experimental band structure 17,23,31,36 agree with the accepted crystal structure of ${\rm TiS_3}$ and ${\rm ZrS_3}$.

Near-edge X-ray absorption fine structure (NEXAFS) or Xray absorption spectroscopy (XAS) and S 2p X-ray photoemission spectroscopy (XPS) were performed using the extremely stable operation conditions of the Synchrotron SOLEIL, which operates in top-up mode which keeps the electron current in the storage ring constant at 500 ± 0.5 mA, ensuring a constant heat load and consequently minimal thermal drifts of the associated optics of the beamline. The beamline is equipped with a set of two complementary insertion devices (the H60 and H256 undulators), in a tandem configuration, delivering a well-established wide spectral distribution with discriminated circular and linear polarization. 44 The ANTARES beamline has a high-energy resolving power (higher than 25000), an excellent harmonic rejection ratio, and a high photon flux of well-controlled polarization light throughout the whole operative energy range from 20 to 1000 eV. 44,45 The NEXAFS/XAS measurements were measured using the total electron yield, where the sample drain current was recorded by a floating nanoampmeter. Measurements were taken on TiS₃ and ZrS₃ nanowhiskers that were exfoliated under vacuum at a base pressure of better than 10⁻¹⁰ Torr. For more experimental details see ref 46.

The sulfur 2p XPS core level spectra of Figure 2a,b were taken using a photon energy of 350 eV. An MBS deflection

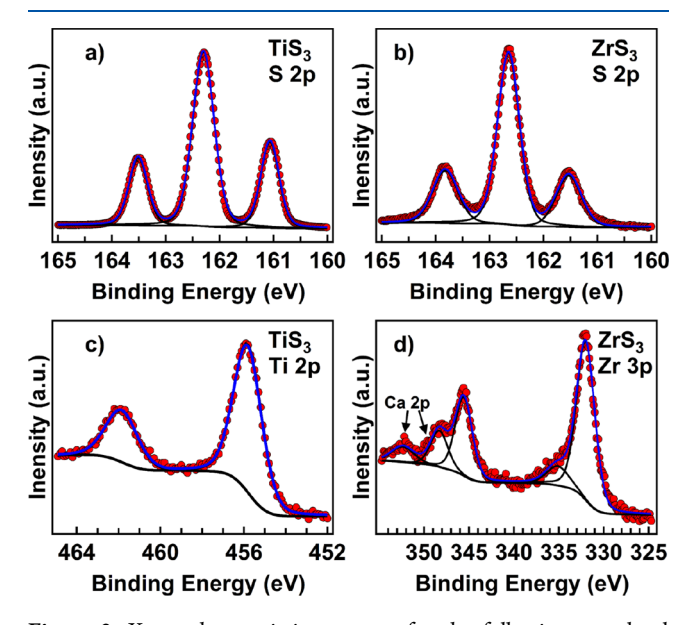


Figure 2. X-ray photoemission spectra for the following core level states: (a) S 2p in TiS_3 , (b) S 2p in ZrS_3 , (c) Ti 2p in TiS_3 , and (d) Zr 3p in ZrS_3 .

analyzer, with an angular and energy resolution of $\sim 0.2^{\circ}$ and ~ 20 meV, respectively, was used for partial photoelectron yield detection in both XPS and XAS taken at SOLEIL. These measurements have been recorded on samples conditioned in an ultrahigh-vacuum chamber (base pressure $\cong 1 \times 10^{-10}$ mbar) at $\alpha = 45^{\circ}$ incidence angle (i.e., electric field vector forms an angle α with the surface normal) with linear horizontal polarization of the light. Spectra were collected at this photon incident angle close to the magic angle (54.8°)

relative to the surface to avoid orientation effects. As an indirect measure of the absorption process, the NEXAFS/XAS spectra were also taken in the partial electron yield (PEY) mode using the MBS electron analyzer, as an additional check. Additional XPS measurements of the Zr 3p and Ti 2p core levels, as in Figure 2c,d, were taken at the University of Nebraska—Lincoln using nonmonochromatized Al K α X-ray radiation. The Ca 2p photoelectron peaks seen in the XPS spectra, evident in Figure 2d, are most likely attributed to CaCO₃ present in the epoxy used to mount the samples. Similarly, the two additional X-ray absorption features seen near photon energies of 348 and 352 eV in Figure 3b are most likely attributed to CaCO₃ present in the epoxy used to mount the samples and resemble previous XAS measurements on the Ca 2p core level edges. 47

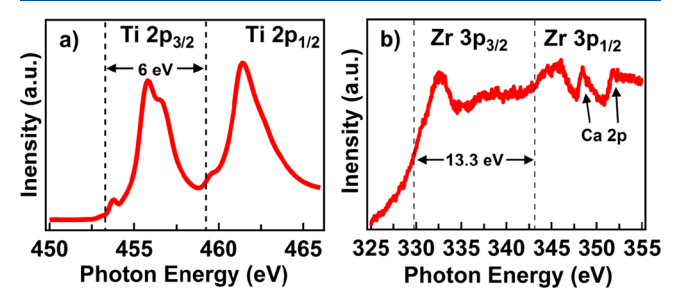


Figure 3. X-ray absorption—NEXAF spectra taken at (a) the Ti 2p edges for TiS₃ and (b) the Zr 3p edges for ZrS₃. Here the data are plotted as a function of incident photon energy. In (b) the likely Ca core level peaks are indicated (see the Methods section).

The nano-angle-resolved photoemission measurements were also performed on the Antares beamline of the synchrotron SOLEIL using a MBS deflection analyzer, with an angular and energy resolution of $\sim\!\!0.2^\circ$ and $\sim\!\!10$ meV, respectively, as successfully demonstrated elsewhere. 23,31,38

2.2. Alignment of Conduction Band in X-ray Absorption. The X-ray absorption spectra are characterized by one or more transitions (absorption edges), where the photon energy position is element specific because this coincides with the energy of the corresponding atomic core level. The X-ray absorption spectra (XAS) taken at the 2p core level edges of Ti for TiS₃, and the 3p edges of Zr, for ZrS₃ are shown in Figures 3a and 3b, respectively, while the XAS spectra taken at the core level 2p edges of S for TiS₃ and ZrS₃ are shown in Figures 4a and 4b, respectively. The Ti 2p_{3/2} and

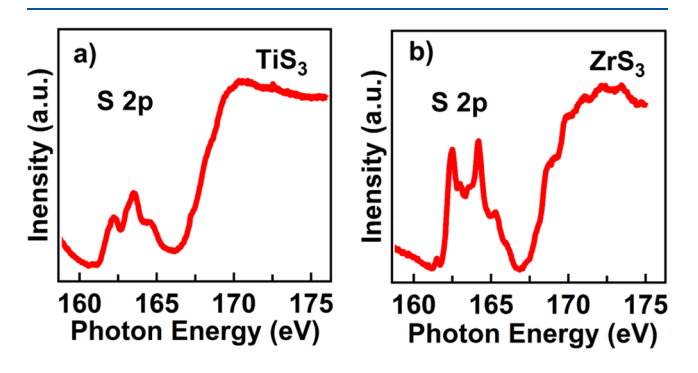


Figure 4. X-ray absorption—NEXAF spectra taken at (a) the S 2p edges for TiS₃ and (b) the S 2p edges for ZrS₃. Here the data are plotted as a function of incident photon energy.

Ti $2p_{1/2}$ absorption edges differ by roughly 6.0 eV (Figure 3a), and the Zr $3p_{3/2}$ and Zr $3p_{1/2}$ absorption edges differ by about 13.6 eV, as seen in Figure 3b. These spin—orbit component separations are consistent with the binding energy shift as is observed in Ti 2p and Zr 3p core level X-ray photoemission shown in Figure 2c,d.

The core level XPS spectra of Figure 3 generally provide reference binding energies to permit alignment of the various core level XAS; i.e., absent any charging, the photon energy in XAS, minus the core level binding energies, sets the placement of the conduction band minimum and states above $E_{\rm F}$, at a particular core edge. In practice, however, it is very challenging for semiconductors and dielectrics due to the potential for sample charging issues, ⁴⁸⁻⁶⁰ final state screening effects, ⁶¹ and configuration interactions to use the X-ray photoemission binding energies, with respect to the Fermi level, to set the position of the conduction band minimum in the same core edge data in X-ray absorption. The S 2p XPS spectra for TiS₃ and ZrS₃ both show triplet-like features with peaks at 161.1, 162.3, and 163.5 eV for TiS₃ and at 161.5, 162.7, and 163.8 eV for ZrS₃. In TiS₃, the Ti $2p_{3/2}$ and $2p_{1/2}$ core level binding energies are 455.9 and 461.9 eV, respectively, and for the ZrS₃, the Zr $3p_{3/2}$ and $3p_{1/2}$ binding energies are 332.1 and 345.7 eV. These values are consistent with previous XPS measurements on $TiS_3^{14,31,39,62-64}$ and ZrS_3^{63-67} Because of the complication just mentioned above and because TiS_3 and ZrS_3 are strongly n-type, using these XPS binding energies is an overestimate of the energy needed to place E_F in the XAS S 2p, Zr 3p, and Ti 2p edges, so discrepancies are addressed by using the onset edges observed in XAS and the Ca 2p edges from the $CaCO_3$ present in the epoxy as a reference in the case of ZrS_3 . Because both $TiS_3^{4,7,14-17,25,31}$ and $ZrS_3^{4,25}$ are strongly n-type materials, with the distance from the valence band to the Fermi level approximately equal to the band gap, 31,38 the onset of states in XAS should occur directly at $E_{\rm f}$. Thus, to place the XAS spectra in the context of the unoccupied states, the Fermi level has been placed at the leading edge of the X-ray absorption envelope grouping of features for each elemental core level studied here, as has been done below (vide infra). In support of this procedure, based on ZrS₃ and TiS₃ being extremely n-type, is the band structure of TiS₃ showing a weak density of states just below the Fermi level, as seen in Figure 5. This weak density of states is donor states indicative of the bottom of the conduction band being placed just above the Fermi level. This band structure is in agreement with prior measurements ^{17,31,38} and the calculated band structure discussed below (vide infra).

The result is that the Ti 2p XAS features are shifted 1–2 eV compared to other XAS studies^{39,40} although the photon energies for the S 2p edge in ZrS₃ presented here appear to be within 1 eV of another XAS study.⁴¹ To the authors knowledge, there are no available XAS studies on the S 2p edge in TiS₃ or the Zr 3p edge in ZrS₃ for comparison.

2.3. Computational Details. The atomic and electronic structures of the TiS_3 and ZrS_3 systems were obtained using density functional theory (DFT) as implemented in the Vienna *ab initio* simulation package (VASP).^{68,69} The projected augmented plane wave (PAW) method is used to approximate the electron—ion potential.⁷⁰ The exchange and correlation potential was calculated using the generalized density approximation (GGA). In these calculations, we used a kinetic energy cutoff of 340 eV for the plane wave expansion of the PAWs and a $6 \times 9 \times 3$ grid of k points⁷¹ for the Brillouin zone

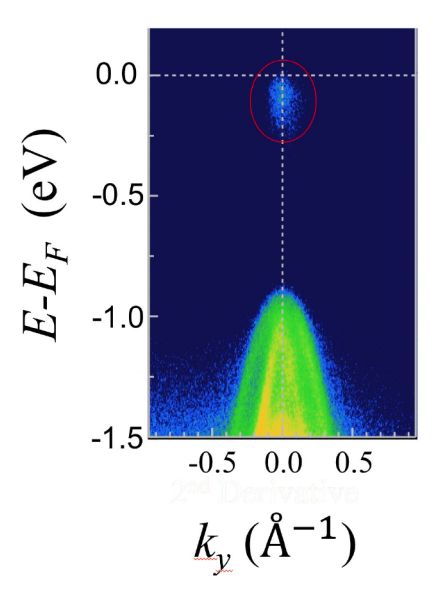


Figure 5. Experimental band structure for $TiS_3(001)$, obtained from angle-resolved photoemission spectroscopy, along the chain direction, i.e., $\overline{\Gamma}$ to \overline{Y} . The red circle indicates a density of states that is not part of the occupied band structure of $TiS_3(001)$, indicative of donor states or the beginning of the bottom of the conduction band.

integration. The exchange and correlation, beyond GGA, were considered by introducing an on-site Coulomb repulsion with a Hubbard U = 6.0 eV for the Ti 3d orbitals in rotationally invariant formalism,⁷² as implemented in VASP, in order to match the calculated band gap. TiS3 can be viewed as $\mathrm{Ti}^{4+}(\mathrm{S_2}^{2-})$ $\mathrm{S^{2-}}$, with $\mathrm{S_2}^{2-}$ forming the edge of the chain perpendicular to the chain direction. 1,15,43 The resulting nonbonding orbitals in that direction lead to highly localized bands seen in valence and conduction bands. The electronic structure, however, was found to be qualitatively similar to those calculations performed without the Hubbard U parameter. For the accurate description of the interlayer separation, the weak interlayer interaction, often termed the van der Waals interaction, was included in the calculations. 73,74 The van der Waals like interaction between 1D chains is important as distance between chains is similar in magnitude (3.4 Å) as the interlayer distance between the planes in graphite. Such interaction in between chains is included in the calculations using DFT-D3 methods.⁷³ Because the materials are n-type, the Fermi level has been positioned at the conduction band minimum.

3. RESULTS AND DISCUSSION

3.1. Conduction Band States of TiS₃. The observed absorption features for the Ti $2p_{3/2}$ and $2p_{1/2}$ states in TiS₃, suitably aligned to the chemical potential, are shown in Figures 6a and 6b, respectively, and are similar to previous studies. The Ti $2p_{3/2}$ and $2p_{1/2}$ absorption spectra were both fit with four peaks. The $2p_{3/2}$ X-ray absorption spectra show features located near 0.5, 1.8, 2.5, and 3.5 eV above the Fermi level, labeled A–D, respectively, when corrected for the core level binding energies. In the $2p_{1/2}$ absorption edge X-ray spectra, peaks were found at 0.3, 1.5, 2.3, and 3.7 eV above the Fermi level, labeled E–H, when suitably corrected for the core level binding energies.

The XAS spectra taken at the sulfur 2p core (Figure 6c), for TiS_3 , are complicated by the proximity of the $2p_{1/2}$ and $2p_{3/2}$

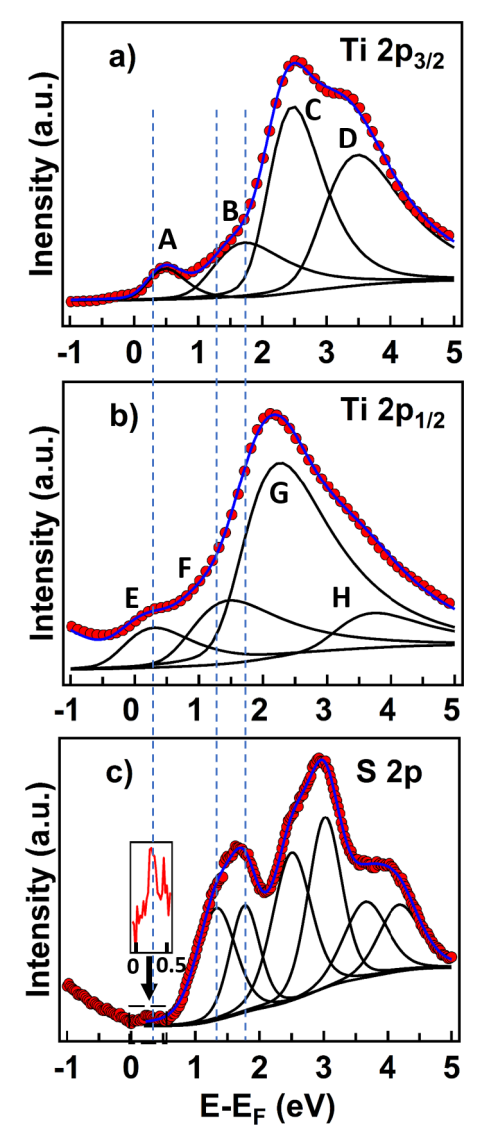


Figure 6. X-ray absorption edges for the (a) Ti $2p_{3/2}$, (b) Ti $2p_{1/2}$, and (c) S 2p excitations in TiS₃. The inset in (c) shows a minor feature located near the Fermi level. The placement of the Fermi level in (c) is valid only for the first occurrence of each conduction band state, whose placement is indicated by the dotted lines. The red circles show experimental data, and the blue and black lines are the results of profile fitting.

core levels, which overlap in binding energy, and the presence of two nonequivalent sulfur sites in TiS_3 . 14,31,39,40,43,62 This gives rise to three separate core level components (due to the overlap of two peaks) for the sulfur 2p electrons in TiS₃, which are separated by a spin-orbit splitting of approximately 1.2 eV, as seen in the core level X-ray photoemission of Figure 2a and discussed above. The placement of the Fermi level, as indicated in Figure 6c, corresponds to the transition from the lowest binding energy S 2p core level state to the conduction band minimum. Although the XAS spectra for the S 2p edge were fit with six peaks, these features are assigned to transitions from the three separate S 2p core level components that occur at different binding energies. Of interest here are the transitions from the S 2p core level with the smallest binding energies to two low-lying unoccupied states in the conduction band at approximately 1.3 and 1.8 eV above the Fermi level. A minor X-ray absorption feature, corresponding to a binding energy of

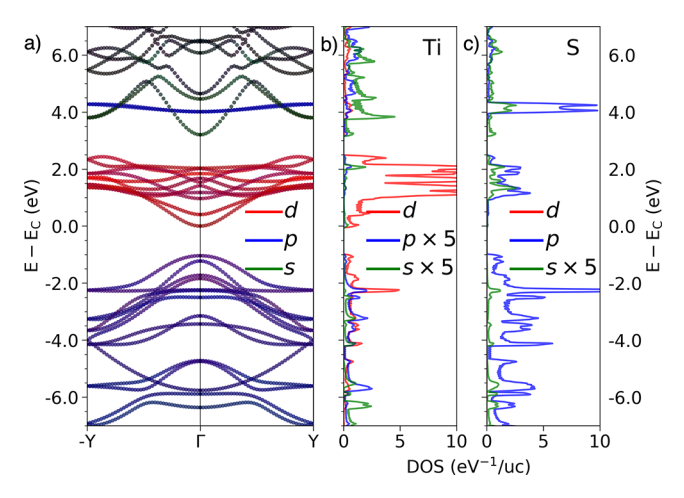


Figure 7. Electronic structure of ${\rm TiS_3}$ bulk (a). The hybridization between Ti-d (red) and S-p (blue) orbitals in the valence and conduction bands is indicated. The bottom of conduction band has mostly Ti-d character. S-p bands start to contribute significantly ~ 1.0 eV above the conduction band minimum. The top of valence band has almost equal contribution from Ti-d and S-p bands. The adjoining orbital resolved partial density of states corresponding to Ti (b) and S (c) show the s orbital contribution (green) is very small around the conduction and valence band edges and has been multiplied by 5 for visualization, as has the Ti-p (b).

around 0.3 eV above the Fermi level, is also seen in the inset of Figure 6c but was not considered in the fitting. The very low intensity of the S core edge XAS features, corresponding to unoccupied states within 1 eV above the relative Fermi level, indicates that the bottom of the conduction band is not strongly sulfur weighted in TiS₃. This is consistent with our theoretical expectations. As seen in Figure 7, the expectation is that the bottom of the conduction band is Ti 3d, with negligible S weight.

The two allowed transitions for the Ti 2p XAS spectra are p \rightarrow s and p \rightarrow d. However, it has been argued that the $2p \rightarrow$ s contributions to the XAS spectra tend to be smaller for strongly ionic 3d compounds. The assignment of the observed transitions to d final states is further supported by the XAS spectra taken at the threshold of the spin—orbit split Ti 2p core, as plotted in Figure 6a,b. While some theoretical calculations predict that the Ti s states will be dominant at the conduction band minimum, as just noted, our theoretical predictions indicate that the bottom of the conduction band is very much dominated by Ti 3d (Figure 7). The very strong Ti $2p_{3/2}$ and $2p_{1/2}$ core X-ray absorption features labeled C and G (in Figure 6) most likely represent transitions to the unoccupied $3d_{5/2}$ and/or $3d_{3/2}$ states. Peaks D and H are expected to be the result of crystal field splitting, which is common in Ti⁴⁺ systems. 75,77,78

From the S 2p core level XAS spectra, in Figure 6c, we find that some features correspond to conduction band states which are aligned with Ti features, in either Figure 6a or 6b, indicative of unoccupied Ti states. This correlation, of S and Ti XAS features, indicates strong S to Ti 3d hybridization within the unoccupied density of states near the Fermi level. The alignment of the Ti 3d and S 3p orbitals approximately from 1 to 2.5 eV above the conduction band minimum has been predicted by theory, 2,5,8 and this is indicated in the calculated band structure and partial density of states for TiS₃, shown in Figure 7. p—d hybridization has been observed for other

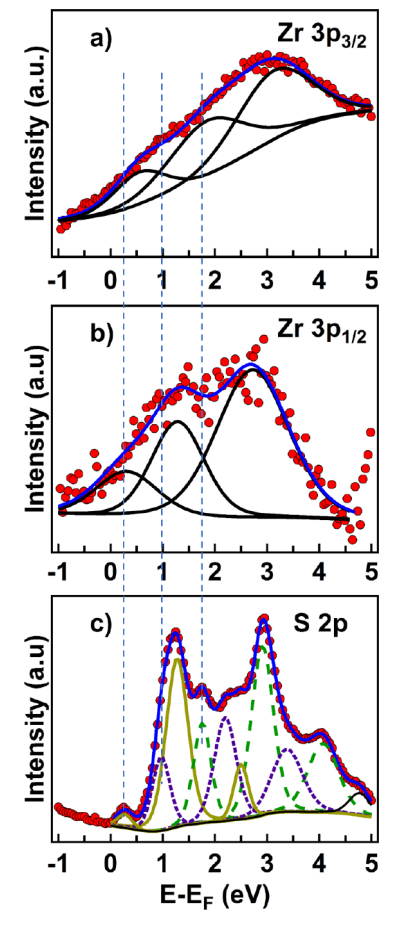


Figure 8. X-ray absorption edges for the (a) Zr $3p_{3/2}$, (b) Zr $3p_{1/2}$, and (c) S 2p excitations in ZrS $_3$. The placement of the Fermi level in (c) is valid only for the first occurrence of each conduction band state indicated by the dotted lines. Green, purple, and gold lines indicate excitations to the same conduction band state from the three distinct core level states.

transition-metal sulfides. 79,80 Thus, the S core edge XAS spectra are likely composed of features resulting from both S 2p \rightarrow unoccupied S 4s–Ti 3d and S 2p \rightarrow unoccupied S 3p–Ti 3d hybridized bands, although theory indicates that the S-s weight to the unoccupied band structure just above the Fermi level is weak (Figure 7). Optically forbidden transitions, such as p-to-p transitions, are allowed if there is hybridization. 81

The calculated TiS₃ band structure (Figure 7) shows clear splitting between two sets of unoccupied bands: lower Ti-d and S-p hybrid bands and upper S-s and S-p hybrid bands. The bottom of the conduction band is mostly dominated by Ti-d bands, as has been noted above. S-p bands start contributing unoccupied density of states about 1 eV above the conduction band minimum and spans the rest of the lower part of the conduction band window. The upper part of the conduction band contains very narrow S-p band and delocalized hybrid S-s and S-p bands. The valence band, on the other hand, is much wider and dominated mostly by S-p and Ti-d orbitals. It should be noted that the top of the valence band is in good agreement with the experimental band structure determined from angle-resolved photoemission ^{17,23,31,38} and Figure 5.

3.2. Conduction Band States of ZrS₃. The XAS spectra taken at the Zr $3p_{3/2}$ and $3p_{1/2}$ core level edges, for ZrS₃, are presented in Figures 8a and 8b, respectively, following alignment with the ZrS₃ Fermi level. Both edges are dominated

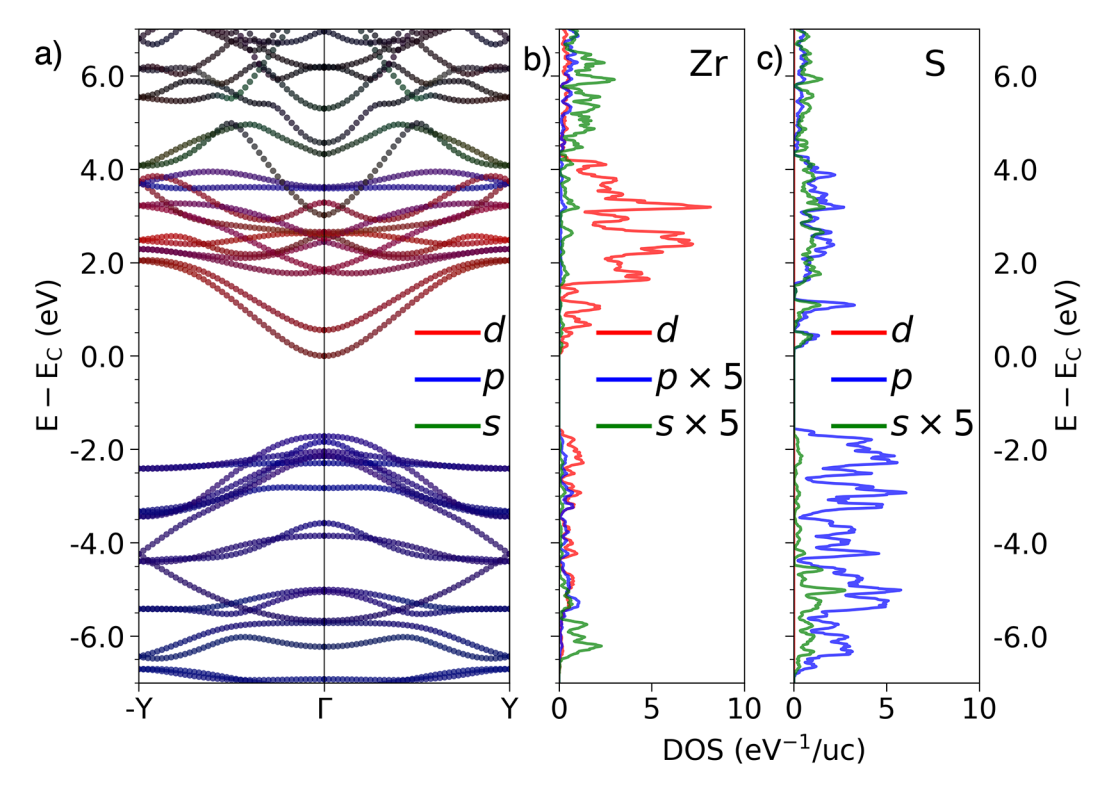


Figure 9. Electronic structure of ZrS_3 bulk (a). The band structure illustrates the hybridization between Zr-d (red) and S-p (blue) orbitals in valence and conduction bands. The bottom of conduction band has mostly Zr-d; however, S-p and S-s orbitals start to contribute immediately above conduction band minimum. The top of valence band has almost equal contributions from Zr-d and S-p bands. The adjoining orbital-resolved partial density of states corresponding to Zr (b) and S (c) shows some S-s (green) and Zr-p orbital contribution to the conduction band edge and has been multiplied by S for visualization.

by a single broad feature which was fit using three peaks located at 0.6, 1.9, and 3.2 eV above the Fermi level for the $3p_{3/2}$ edge and at 0.3, 1.3, and 2.7 eV for the $3p_{1/2}$. As with the Ti 2p core level XAS features for TiS₃, the Zr transitions evident in Figure 8a,b are expected to be dominated by $p \rightarrow d$ transitions as indicated in the calculated partial density of states for the conduction band region of ZrS₃, as seen in Figure

The XAS spectrum taken at the S 2p core level edge, for ZrS₃, is shown in Figure 8c. Similar to the S 2p edge in TiS₃, the S 2p edge in ZrS₃ shows unoccupied S weighted states at roughly 0.3, 1.0, and 1.8 eV above the Fermi level. However, unlike in TiS₃, the transition to the state 0.3 eV above the Fermi level is significant. Because of this, the profile fitting requires three triplets rather than two. The three triplets are separated by 1.1–1.2 eV, which is consistent with the separation between the core level states observed by XPS in Figure 2b, as previously discussed. An additional tenth peak was required to fit a small shoulder feature at 4.8 eV in the XAS spectra.

The calculated ZrS_3 band structure (Figure 9) shows a single wide conduction band with the bandwidth of the lower part of the conduction band now \sim 4 to 5 eV. The conduction band is dominated by Zr-d orbitals, even though S-s and S-p contribute. The S-s and S-p orbitals start contributing immediately above the conduction band minimum, more significantly by the latter. The valence band, on the other hand, is dominated by the S-p orbital, even though Zr-d orbitals make significant contributions to the valence band as well. The band structure at the top of the valence band qualitatively

agrees with the experimental band structure for ZrS₃³⁸ and is consistent with the occupied band structure of TiS₃. ^{17,23,31,38}

As with TiS_3 , the three S-weighted conduction band states of ZrS_3 appear hybridized with the transition-metal orbitals based on their energy alignment indicating either S $2p \rightarrow S$ 4s-Zr 4d or S $2p \rightarrow S$ 3p-Zr 4d transitions. The S 2p XAS transition to the unoccupied state near the Fermi level has a more significant intensity for ZrS_3 (Figure 8c) than for TiS_3 (Figure 6c) where this transition to a similar unoccupied state near the Fermi level is barely evident. This indicates that the conduction band minimum in ZrS_3 contains more sulfur weight than is the case for TiS_3 . This is consistent with our theoretical expectations (Figure 9).

4. CONCLUSIONS

As expected, the unoccupied states in the vicinity of the Fermi level of the conduction bands of TiS₃ and ZrS₃ are qualitatively similar. This was shown using X-ray absorption spectroscopy taken at the 2p core level edges of Ti and S, for TiS₃, and at the core level 2p edges of S and 3p edges of Zr, for ZrS₃. For both TiS₃ and ZrS₃, the unoccupied states of the conduction band within 2 eV of the Fermi level appear dominated by either S s to Ti/Zr d or S p to Ti/Zr d hybridized orbitals. This sulfur-to-metal hybridization that has been now established experimentally for the conduction band is expected to result in a partially delocalized electronic distribution between the Ti and S atoms within the same 1D chains, consistent with previous predictions. The S atoms in both TiS₃ and ZrS₃ contribute appreciably to the electronic configuration between 1 and 2 eV above the Fermi level, but within 1 eV of the Fermi level the S

contributions to the conduction band are very weak for TiS_3 and stronger for ZrS_3 .

AUTHOR INFORMATION

Corresponding Author

Peter A. Dowben – Department of Physics and Astronomy, University of Nebraska—Lincoln, Lincoln, Nebraska 68588-0299, United States; ⊚ orcid.org/0000-0002-2198-4710; Email: pdowben1@unl.edu

Authors

- Simeon J. Gilbert Department of Physics and Astronomy, University of Nebraska—Lincoln, Lincoln, Nebraska 68588-0299, United States
- **Hemian Yi** Synchrotron SOLEIL and Universite Paris-Saclay, 91190 Saint-Aubin, France
- Tula Paudel Department of Physics and Astronomy, University of Nebraska—Lincoln, Lincoln, Nebraska 68588-0299, United States; Department of Physics, South Dakota School of Mines and Technology, Rapid City, South Dakota 57701-3901, United States
- Alexey Lipatov Department of Chemistry, University of Nebraska—Lincoln, Lincoln, Nebraska 68588-0304, United States; orcid.org/0000-0001-5043-1616
- Andrew J. Yost Department of Physics and Astronomy, University of Nebraska—Lincoln, Lincoln, Nebraska 68588-0299, United States; orcid.org/0000-0002-6220-7520
- Alexander Sinitskii Department of Chemistry, University of Nebraska—Lincoln, Lincoln, Nebraska 68588-0304, United States; Nebraska Center for Materials and Nanoscience, University of Nebraska—Lincoln, Lincoln, Nebraska 68588-0298, United States; orcid.org/0000-0002-8688-3451
- Evgeny Y. Tsymbal Department of Physics and Astronomy, University of Nebraska—Lincoln, Lincoln, Nebraska 68588-0299, United States; orcid.org/0000-0002-6728-5480
- Jose Avila Synchrotron SOLEIL and Universite Paris-Saclay, 91190 Saint-Aubin, France
- Maria C. Asensio Madrid Institute of Materials Science (ICMM), Spanish Scientific Research Council (CSIC), E-28049 Madrid, Spain; o orcid.org/0000-0001-8252-7655

Complete contact information is available at: https://pubs.acs.org/10.1021/acs.jpcc.2c05589

Notes

The authors declare no competing financial interest.

ACKNOWLEDGMENTS

This research was supported by the National Science Foundation through EPSCoR RII Track-1: Emergent Quantum Materials and Technologies (EQUATE), Award OIA-2044049. The Synchrotron SOLEIL was supported by the Centre National de la Recherche Scientifique (CNRS) and the Commissariat à l'Energie Atomique et aux Energies Alternatives (CEA), France. This work was also supported by a public grant by the French National Research Agency (ANR) as part of the "Investissements d'Avenir" (reference: ANR-17-CE09-0016-05). The work at the South Dakota School of Mines and Technology is supported by the South Dakota Board of Reagents, Research initiation grant MA2200010. Significant portions of this paper have been adopted from Chapter 5, of Simeon Gilbert's doctoral thesis "The Electronic Properties Of The Quasi-One-Dimensional TiS₃ And ZrS₃", 2020, University of Nebraska.

REFERENCES

- (1) Lipatov, A.; Loes, M. J.; Lu, H.; Dai, J.; Patoka, P.; Vorobeva, N. S.; Muratov, D. S.; Ulrich, G.; Kästner, B.; Hoehl, A.; et al. Quasi-1D TiS₃ Nanoribbons: Mechanical Exfoliation and Thickness-Dependent Raman Spectroscopy. *ACS Nano* **2018**, *12*, 12713–20.
- (2) Dai, J.; Zeng, X. C. Titanium trisulfide monolayer: Theoretical prediction of a new direct-gap semiconductor with high and anisotropic carrier mobility. *Angew. Chemie Int. Ed.* **2015**, *54*, 7572–6.
- (3) Ferrer, I. J.; Ares, J. R.; Clamagirand, J. M.; Barawi, M.; Sánchez, C. Optical properties of titanium trisulphide (TiS_3) thin films. *Thin Solid Films* **2013**, 535, 398–401.
- (4) Flores, E.; Ares, J. R.; Ferrer, I. J.; Sánchez, C. Synthesis and characterization of a family of layered trichalcogenides for assisted hydrogen photogeneration. *Phys. Status Solidi Rapid Res. Lett.* **2016**, 10, 802–6.
- (5) Liu, S.; Xiao, W.; Zhong, M.; Pan, L.; Wang, X.; Deng, H.-X.; Liu, J.; Li, J.; Wei, Z. Highly polarization sensitive photodetectors based on quasi-1D titanium trisulfide (TiS₃). *Nanotechnology* **2018**, 29, 184002.
- (6) Island, J. O.; Biele, R.; Barawi, M.; Clamagirand, J. M.; Ares, J. R.; Sánchez, C.; van der Zant, H. S. J.; Ferrer, I. J.; D'Agosta, R.; Castellanos-Gomez, A. Titanium trisulfide (TiS₃): A 2D semiconductor with quasi-1D optical and electronic properties. *Sci. Rep.* **2016**, *6*, 22214.
- (7) Island, J. O.; Barawi, M.; Biele, R.; Almazán, A.; Clamagirand, J. M.; Ares, J. R.; Sánchez, C.; van der Zant, H. S. J.; Álvarez, J. V.; D'Agosta, R.; et al. TiS₃ transistors with tailored morphology and electrical properties. *Adv. Mater.* **2015**, *27*, 2595–601.
- (8) Taniguchi, K.; Gu, Y.; Katsura, Y.; Yoshino, T.; Takagi, H. Rechargeable Mg battery cathode TiS₃ with d-p orbital hybridized electronic structures. *Appl. Phys. Express* **2016**, *9*, 011801.
- (9) Iyikanat, F.; Senger, R. T.; Peeters, F. M.; Sahin, H. Quantum-Transport Characteristics of a p-n Junction on Single-Layer TiS₃. *ChemPhysChem* **2016**, *17*, 3985–91.
- (10) Silva-Guillén, J. A.; Canadell, E.; Ordejón, P.; Guinea, F.; Roldán, R. Anisotropic features in the electronic structure of the two-dimensional transition metal trichalcogenide TiS₃: Electron doping and plasmons. 2D Mater. **2017**, *4*, 025085.
- (11) Island, J. O.; Buscema, M.; Barawi, M.; Clamagirand, J. M.; Ares, J. R.; Sánchez, C.; Ferrer, I. J.; Steele, G. A.; van der Zant, H. S. J.; Castellanos-Gomez, A. Ultrahigh photoresponse of few-layer TiS₃ nanoribbon transistors. *Adv. Opt. Mater.* **2014**, *2*, 641–5.
- (12) Ferrer, I. J.; Maciá, M. D.; Carcelén, V.; Ares, J. R.; Sánchez, C. On the photoelectrochemical properties of TiS₃ films. *Energy Procedia* **2012**, 22, 48–52.
- (13) Cui, Q.; Lipatov, A.; Wilt, J. S.; Bellus, M. Z.; Zeng, X. C.; Wu, J.; Sinitskii, A.; Zhao, H. Time-Resolved Measurements of Photocarrier Dynamics in TiS₃ Nanoribbons. *ACS Appl. Mater. Interfaces* **2016**, *8*, 18334–8.
- (14) Gilbert, S. J.; Lipatov, A.; Yost, A. J.; Loes, M. J.; Sinitskii, A.; Dowben, P. A. The electronic properties of Au and Pt metal contacts on quasi-one-dimensional layered TiS₃ (001). *Appl. Phys. Lett.* **2019**, *114*, 101604.
- (15) Lipatov, A.; Wilson, P. M.; Shekhirev, M.; Teeter, J. D.; Netusil, R.; Sinitskii, A. Few-layered titanium trisulfide (TiS₃) field-effect transistors. *Nanoscale* **2015**, *7*, 12291–6.
- (16) Molina-Mendoza, A. J.; Island, J. O.; Paz, W. S.; Clamagirand, J. M.; Ares, J. R.; Flores, E.; Leardini, F.; Sánchez, C.; Agrait, N.; Rubio-Bollinger, G.; et al. High Current Density Electrical Breakdown of TiS₃ Nanoribbon-Based Field-Effect Transistors. *Adv. Funct. Mater.* **2017**, *27*, 1605647.
- (17) Randle, M.; Lipatov, A.; Kumar, A.; Kwan, C.-P.; Nathawat, J.; Barut, B.; Yin, S.; He, K.; Arabchigavkani, N.; Dixit, R.; et al. Gate-Controlled Metal—Insulator Transition in TiS₃ Nanowire Field-Effect Transistors. *ACS Nano* **2019**, *13*, 803–11.
- (18) Galiy, P. V.; Randle, M.; Lipatov, A.; Wang, L.; Gilbert, S.; Vorobeva, N.; Kumar, A.; Kwan, C.-P.; Nathawat, J.; Barut, B.; et al. Building the Quasi one Dimensional Transistor from 2D Materials.

- IEEE 2nd Ukraine Conf. on Electrical and Computer Engineering 2019, 679-682.
- (19) Island, J. O.; Molina-Mendoza, A. J.; Barawi, M.; Biele, R.; Flores, E.; Clamagirand, J. M.; Ares, J. R.; Sánchez, C.; van der Zant, H. S. J.; D'Agosta, R.; et al. Electronics and optoelectronics of quasi-1D layered transition metal trichalcogenides. 2D Mater. 2017, 4, 022003.
- (20) Patra, A.; Rout, C. S. Anisotropic quasi-one-dimensional layered transition-metal trichalcogenides: synthesis, properties and applications. *RSC Adv.* **2020**, *10*, 36413.
- (21) Niu, Y.; Frisenda, R.; Flores, E.; Ares, J. R.; Jiao, W.; de Perez, L. D.; Sánchez, C.; Wang, R.; Ferrer, I. J.; Castellanos-Gomez, A. Polarization-Sensitive and Broadband Photodetection Based on a Mixed-Dimensionality TiS₃/Si p-n Junction. *Adv. Opt. Mater.* **2018**, *6*, 1800351.
- (22) Talib, M.; Tabassum, R.; Abid; Islam, S. S.; Mishra, P. Improvements in the Performance of a Visible–NIR Photodetector Using Horizontally Aligned TiS₃ Nanoribbons. *ACS Omega* **2019**, *4*, 6180–91.
- (23) Gilbert, S. J.; Yi, H.; Chen, J.-S.; Yost, A. J.; Dhingra, A.; Abourahma, J.; Lipatov, A.; Avila, J.; Komesu, T.; Sinitskii, A.; et al. The Effect of Band Symmetry on Photocurrent Production in the Quasi-One-Dimensional Transition Metal Trichalcogenides. *ACS Appl. Mater. Interfaces* **2020**, *12*, 40525–40531.
- (24) Jin, H.; Cheng, D.; Li, J.; Cao, X.; Li, B.; Wang, X.; Liu, X.; Zhao, X. Facile synthesis of zirconium trisulfide and hafnium trisulfide nanobelts: Growth mechanism and Raman spectroscopy. *Solid State Sci.* **2011**, *13*, 1166–71.
- (25) Morozova, N. V.; Korobeinikov, I. V.; Kurochka, K. V.; Titov, A. N.; Ovsyannikov, S. V. Thermoelectric Properties of Compressed Titanium and Zirconium Trichalcogenides. *J. Phys. Chem. C* **2018**, 122, 14362—72.
- (26) Pant, A.; Torun, E.; Chen, B.; Bhat, S.; Fan, X.; Wu, K.; Wright, D. P.; Peeters, F. M.; Soignard, E.; Sahin, H.; Tongay, S. Strong dichroic emission in the pseudo one dimensional material ZrS₃. *Nanoscale* **2016**, *8*, 16259–65.
- (27) Wu, J. J.; Tao, Y. R.; Wang, J. N.; Wu, Z. Y.; Fan, L.; Wu, X. C. Reverse saturable absorption and nonlinear refraction of ultrathin ZrS₃ nanobelts. *Nanoscale* **2016**, *8*, 10371–9.
- (28) Xiong, W.-W.; Chen, J.-Q.; Wu, X.-C.; Zhu, J.-J. Individual HfS₃ nanobelt for field-effect transistor and high performance visible-light detector. *J. Mater. Chem. C* **2014**, *2*, 7392.
- (29) Tao, Y. R.; Wu, J. J.; Wu, X. C. Enhanced ultraviolet-visible light responses of phototransistors based on single and a few ZrS₃ nanobelts. *Nanoscale* **2015**, *7*, 14292–8.
- (30) Zybtsev, S. G.; Pokrovskii, V. YA.; Nasretdinova, V. F.; Zaitsev-Zotov, S. V.; Pavlovskiy, V. V.; Odobesco, A. B.; Wu, P. W.; Chu, M.; Lin, Y. G.; Zupanič, E. P.; et al. NbS₃: A unique quasi-one-dimensional conductor with three charge density wave transitions. *Phys. Rev. B* **2017**, *95*, 35110.
- (31) Yi, H.; Komesu, T.; Gilbert, S.; Hao, G.; Yost, A. J.; Lipatov, A.; Sinitskii, A.; Avila, J.; Chen, C.; Asensio, M. C.; Dowben, P. A. The band structure of the quasi-one-dimensional layered semiconductor TiS₃(001). *Appl. Phys. Lett.* **2018**, *112*, 052102.
- (32) Wang, X.; Wu, K.; Blei, M.; Wang, Y.; Pan, L.; Zhao, K.; Shan, C.; Lei, M.; Cui, Y.; Chen, B.; Wright, D.; Hu, W.; Tongay, S.; Wei, Z. Highly Polarized Photoelectrical Response in VdW ZrS₃ Nanoribbons. *Adv. Electron. Mater.* **2019**, *5*, 1900419.
- (33) Kong, W.; Bacaksiz, C.; Chen, B.; Wu, K.; Blei, M.; Fan, X.; Shen, Y.; Sahin, H.; Wright, D.; Narang, D. S.; Tongay, S. Angle Resolved Vibrational Properties of Anisotropic Transition Metal Trichalcogenide Nanosheets. *Nanoscale* **2017**, *9*, 4175–4182.
- (34) Yang, S.; Wu, M.; Shen, W.; Huang, L.; Tongay, S.; Wu, K.; Wei, B.; Qin, Y.; Wang, Z.; Jiang, C.; Hu, C. Highly Sensitive Polarization Photodetection Using a Pseudo-One-Dimensional Nb_(1-x)TixS₃ Alloy. ACS Appl. Mater. Interfaces **2019**, 11, 3342–3352.
- (35) Khatibi, A.; Godiksen, R. H.; Basuvalingam, S. B.; Pellegrino, D.; Bol, A. A.; Shokri, B.; Curto, A. G. Anisotropic Infrared Light Emission from Quasi-1D Layered TiS₃. 2D Mater. **2020**, 7, 015022.

- (36) Papadopoulos, N.; Frisenda, R.; Biele, R.; Flores, E.; Ares, J. R.; Sánchez, C.; van der Zant, H. S. J.; Ferrer, I. J.; D'Agosta, R.; Castellanos-Gomez, A. Large Birefringence and Linear Dichroism in TiS₃ Nanosheets. *Nanoscale* **2018**, *10*, 12424–12429.
- (37) Vorobeva, N.; Lipatov, A.; Torres, A.; Dai, J.; Abourahma, J.; Le, D.; Dhingra, A.; Gilbert, S.; Galiy, P.; Nenchuk, T.; et al. Highly Anisotropic Properties of Quasi-1D In₄Se₃: Mechanical Exfoliation, Electronic Transport and Fast Polarization-Dependent Photoresponse. *Adv. Funct. Mater.* **2021**, *31*, 2106459.
- (38) Yi, H.; Gilbert, S. J.; Lipatov, A.; Sinitskii, A.; Avila, J.; Abourahma, J.; Komesu, T.; Asensio, M. C.; Dowben, P. A. The electronic band structure of quasi-one-dimensional van der Waals semiconductors: the effective hole mass of ZrS₃ compared to TiS₃. *J. Phys.: Condens. Matter* **2020**, 32, 29LT01.
- (39) Fleet, M. E.; Harmer, S. L.; Liu, X.; Nesbitt, H. W. Polarized X-ray absorption spectroscopy and XPS of TiS₃: S K- and Ti L-edge XANES and S and Ti 2p XPS. *Surf. Sci.* **2005**, *584*, 133–45.
- (40) Shkvarin, A. S.; Yarmoshenko, Y. M.; Yablonskikh, M. V.; Merentsov, A. I.; Titov, A. N. An X-ray spectroscopy study of the electronic structure of TiS₃. *J. Struct. Chem.* **2014**, *55*, 1039–43.
- (41) Chen, J. G. NEXAFS investigations of transition metal oxides, nitrides, carbides, sulfides and other interstitial compounds. *Surf. Sci. Rep.* **1997**, 30, 117.
- (42) Borca, C. N.; Komesu, T.; Jeong, H. K.; Dowben, P. A.; Ristoiu, D.; Hordequin, Ch.; Nozières, J. P.; Pierre, J.; Stadler, S.; Idzerda, Y. U. Evidence for Temperature Dependent Moment ordering in Ferromagnetic NiMnSb(100). *Phys. Rev. B* **2001**, *64*, 052409.
- (43) Furuseth, S.; Brattas, L.; Kjekshus, A.; Andresen, A. F.; Fischer, P. On the Crystal Structures of TiS₃, ZrS₃, ZrSe₃, ZrTe₃, HfS₃, and HfSe₃. *Acta Chemica Scandinavica A* **1975**, 29, 623–631.
- (44) Avila, J.; et al. ANTARES, a scanning photoemission microscopy beamline at SOLEIL. *Journal of Physics: Conference Series* **2013**, 425, 192023–4.
- (45) Avila, J.; Asensio, M. C. First NanoARPES User Facility Available at SOLEIL: An Innovative and Powerful Tool for Studying Advanced Materials. *Synchrotron Radiation News* **2014**, 27, 24–30.
- (46) Chen, C.; Avila, J.; Frantzeskakis, E.; Levy, A.; Asensio, M. C. Observation of a two-dimensional liquid of Fröhlich polarons at the bare SrTiO₃ surface. *Nat. Commun.* **2015**, *6*, 8585.
- (47) McLeod, J. A.; Buling, A.; Kurmaev, E. Z.; Sushko, P. V.; Neumann, M.; Finkelstein, L. D.; Kim, S.-W.; Hosono, H.; Moewes, A. Spectroscopic characterization of a multiband complex oxide: Insulating and conducting cement 12CaO·7Al₂O₃. *Phys. Rev. B* **2012**, 85, 045204.
- (48) Cazaux, J. Mechanisms of charging in electron spectroscopy. J. Electron Spectrosc. Relat. Phenom. 1999, 105, 155–185.
- (49) Cazaux, J. About the charge compensation of insulating samples in XPS. J. Electron Spectrosc. Relat. Phenom. 2000, 113, 15–33.
- (50) Baer, D. R.; Artyushkova, K.; Cohen, H.; Easton, C. D.; Engelhard, M.; Gengenbach, T. R.; Greczynski, G.; Mack, P.; Morgan, D. J.; Roberts, A. XPS guide: Charge neutralization and binding energy referencing for insulating samples. *J. Vac. Sci. Technol. A* **2020**, 38, 031204.
- (51) Tasci, T. O.; Atalar, E.; Demirok, U. K.; Suzer, S. Electrical circuit modeling of surface structures for X-ray photoelectron spectroscopic measurements. *Surf. Sci.* **2008**, *602*, 365–368.
- (52) Ertas, G.; Demirok, U. K.; Atalar, A.; Suzer, S. X-ray photoelectron spectroscopy for resistance-capacitance measurements of surface structures". *Appl. Phys. Lett.* **2005**, *86*, 183110.
- (53) Barr, T. L. Studies in differential charging. J. Vac. Sci. Technol. A 1989, 7, 1677.
- (54) Tielsch, B. J.; Fulghum, J. E. Differential Charging in XPS. Part I: Demonstration of Lateral Charging in a Bulk Insulator Using Imaging XPS. *Surf. Interface Anal.* **1996**, 24, 422.
- (55) Tielsch, B. J.; Fulghum, J. E.; Surman, D. J. Differential Charging in XPS. Part 11. Sample Mounting and X-ray Flux Effects on Heterogeneous Samples. *Surf. Interface Anal.* **1996**, *24*, 459.
- (56) Wooten, D.; Ketsman, I.; Xiao, J.; Losovyj, Y. B.; Petrosky, J. C.; McClory, J.; Burak, Y.; Adamiv, V.; Dowben, P. A Differences in

- the Surface Charging at the (100) and (110) Surfaces of $\text{Li}_2\text{B}_4\text{O}_{7}$, Nuclear Radiation Detection Materials. *Mater. Res. Soc. Symp. Proc.* **2009**, 1164, L04–04.
- (57) Ketsman, I.; Wooten, D.; Xiao, J.; Losovyj, Ya. B.; Burak, Ya. V.; Adamiv, V. T.; Sokolov, A.; Petrosky, J.; McClory, J.; Dowben, P. A. The off-axis pyroelectric effect observed for lithium tetraborate. *Phys. Lett. Sect. A* **2010**, *374*, 891–895.
- (58) Xiao, J.; Lozova, N.; Losovyj, Ya. B.; Wooten, D.; Ketsman, I.; Swinney, M. W.; Petrosky, J.; McClory, J.; Burak, Ya. V.; Adamiv, V. T.; et al. Surface Charging at the (100) Surface of Cu doped and undoped Li₂B₄O₇. *Appl. Surf. Sci.* **2011**, 257, 3399–3403.
- (59) Adamiv, V. T.; Burak, Ya. V.; Wooten, D.; McClory, J.; Petrosky, J.; Ketsman, I.; Xiao, J.; Losovyj, Ya. B.; Dowben, P. A. The Electronic Structure and Secondary Pyroelectric Properties of Lithium Tetraborate. *Materials* **2010**, *3*, 4550–4579.
- (60) Dugan, C.; Hengehold, R. L.; McHale, S. R.; Colón Santana, J. A.; McClory, J. W.; Adamiv, V. T.; Burak, Ya. V.; Losovyj, Ya. B.; Dowben, P. A. Reversible Mn Segregation at the Polar Surface of Lithium Tetraborate. *Appl. Phys. Lett.* **2013**, *102*, 161602.
- (61) Dowben, P. A. The Metallicity of Thin Films and Overlayers. Surf. Sci. Rep. 2000, 40, 151–247.
- (62) Endo, K.; Ihara, H.; Watanabe, K.; Gonda, S.-I. XPS study of one-dimensional compounds: TiS₃. *J. Solid State Chem.* **1982**, 44, 268–72.
- (63) Dhingra, A.; Lipatov, A.; Loes, M. J.; Sinitskii, A.; Dowben, P. A. The Nonuniform Debye Temperatures in Quasi-One-Dimensional Transition-Metal Trichalcogenides. *ACS Materials Lett.* **2021**, *3*, 414–419.
- (64) Dhingra, A.; Nikonov, D. E.; Lipatov, A.; Sinitskii, A.; Dowben, P. A. What happens when transition metal trichalcogenides are interfaced with gold? *J. Mater. Res.* **2022**, DOI: 10.1557/s43578-022-00744-6.
- (65) Dhingra, A.; Lipatov, A.; Sinitskii, A.; Dowben, P. A. Complexities at the Au/ZrS₃(001) interface probed by X-ray photoemission spectroscopy. *J. Phys.: Condens. Matter* **2021**, 33, 434001.
- (66) Jellinek, F.; Pollak, R. A.; Shafer, M. W. X-ray photoelectron spectra and electronic structure of zirconium trisulfide and triselenide. *Mater. Res. Bull.* **1974**, *9*, 845–56.
- (67) Artemkina, S.; Poltarak, A.; Poltarak, P.; Asanov, I.; Fedorov, V. Photodecoloration of Methyl Orange Solution Assisted by ZrS₃ Powders. *Advances in Science, Technology and Engineering Systems Journal* **2019**, *4*, 165–170.
- (68) Kresse, G.; Furthmüller, J. Efficient iterative schemes for ab initio total-energy calculations using a plane-wave basis set. *Phys. Rev. B* **1996**, *54*, 11169–11186.
- (69) Kresse, G.; Joubert, D. From ultrasoft pseudopotentials to the projector augmented-wave method. *Phys. Rev. B* **1999**, *59*, 1758–1775.
- (70) Blöchl, P. E. Projector augmented-wave method. *Phys. Rev. B* **1994**, *50*, 17953–17979.
- (71) Monkhorst, H. J.; Pack, J. D. Special points for Brillouin-zone integrations. *Phys. Rev. B* **1976**, *13*, 5188–5192.
- (72) Dudarev, S. L.; Botton, G. A.; Savrasov, S. Y.; Humphreys, C. J.; Sutton, A. P. Electron-energy-loss spectra and the structural stability of nickel oxide: An LSDA+U study. *Phys. Rev. B* **1998**, *57*, 1505–1509.
- (73) Grimme, S.; Antony, J.; Ehrlich, S.; Krieg, H. A Consistent and Accurate *Ab Initio* Parametrization of Density Functional Dispersion Correction (DFT-D) for the 94 Elements H–Pu. *J. Chem. Phys.* **2010**, 132 (15), 154104.
- (74) Grimme, S.; Ehrlich, S.; Goerigk, L. Effect of the Damping Function in Dispersion Corrected Density Functional Theory. *J. Comput. Chem.* **2011**, 32 (7), 1456–1465.
- (75) van der Laan, G.; Kirkman, I. W. The 2p absorption spectra of 3d transition metal compounds in tetrahedral and octahedral symmetry. *J. Phys.: Condens. Matter* **1992**, *4*, 4189–204.

- (76) Abdulsalam, M.; Joubert, D. P. Structural and electronic properties of MX_3 (M = Ti, Zr and Hf; X = S, Se, Te) from first principles calculations. *Eur. Phys. J. B* **2015**, *88*, 177.
- (77) de Groot, F. M. F.; Fuggle, J. C.; Thole, B. T.; Sawatzky, G. A. $L_{2,3}$ x-ray-absorption edges of d^0 compounds: K^+ , Ca^{2+} , Sc^{3+} , and Ti^{4+} in O_h (octahedral) symmetry. *Phys. Rev. B* **1990**, *41*, 928–37.
- (78) de Groot, F. M. F.; Fuggle, J. C.; Thole, B. T.; Sawatzky, G. A. 2p x-ray absorption of 3d transition-metal compounds: An atomic multiplet description including the crystal field. *Phys. Rev. B* **1990**, *42*, 5459–68.
- (79) Soldatov, A. V.; Kravtsova, A. N.; Fleet, M. E.; Harmer, S. L. Electronic structure of MeS (Me = Ni,Co,Fe): x-ray absorption analysis. *J. Phys.: Condens. Matter* **2004**, *16*, 7545–56.
- (80) Tossell, J. A. SCF– $X\alpha$ scattered wave MO studies of the electronic structure of ferrous iron in octahedral coordination with sulfur. *J. Chem. Phys.* **1977**, *66*, 5712–9.
- (81) Sakisaka, Y.; Rhodin, T. N.; Dowben, P. A. Resonant Photoemission at the 3s Threshold of Ni. *Solid State Commun.* **1984**, 49, 563–565.

□ Recommended by ACS

Density Functional Theory Study of Two-Dimensional Post-Transition Metal Chalcogenides and Halides for Interfacial Charge Transport in Perovskite Solar Cells

Sri Kasi Matta, Salvy P. Russo, et al.

SEPTEMBER 20, 2022

ACS APPLIED NANO MATERIALS

READ 🗹

Healing Se Vacancies in Bi₂Se₃ by Ambient Gases

Sharmila N. Shirodkar, Pratibha Dev, et al.

SEPTEMBER 21, 2022

THE JOURNAL OF PHYSICAL CHEMISTRY C

READ 🗹

Giant Thermoelectric Power Factor Anisotropy in PtSb_{1.4}Sn_{0.6}

Yu Liu, Cedomir Petrovic, et al.

AUGUST 16, 2022

INORGANIC CHEMISTRY

READ 🗹

Effect of the Titanium Self-Intercalation on the Electronic Structure of TiSe,

Alexey S. Shkvarin, Alexander N. Titov, et al.

DECEMBER 15, 2020

INORGANIC CHEMISTRY

READ 🗹

Get More Suggestions >